Stretching-induced interconnect delamination in stretchable electronic circuits

O van Der Sluis, y y Hsu, P H M Timmermans, M Gonzalez, J P M Hoefnagels

Stretching induced interconnect delamination in stretchable electronic circuits

O van der Sluis[1,2], Y Y Hsu[3,4], P H M Timmermans[1], M Gonzalez[3] and J P M Hoefnagels[2]

[1] Philips Applied Technologies, High Tech Campus 7, 5656 AE Eindhoven, NL
[2] Eindhoven University of Technology, 5600 MB Eindhoven, NL
[3] IMEC INTPAC/REMO, Kapeldreef 75, 3001 Leuven, BE
[4] Katholieke Universiteit Leuven, Oude Markt 13, 3000 Leuven, BE

E-mail: olaf.van.der.sluis@philips.com

Abstract. Stretchable electronics offer increased design freedom of electronic products. Typically, small rigid semiconductor islands are interconnected with thin metal conductor lines on top of, or encapsulated in, a highly compliant substrate, such as a rubber material. A key requirement is large stretchability, i.e. the ability to withstand large deformations during usage without any loss of functionality. Stretching induced delamination is one of the major failure modes that determines the amount of stretchability that can be achieved for a given interconnect design. During peel testing, performed to characterize the interface behaviour, the rubber is severely lifted at the delamination front while at the same time fibrillation of the rubber at the peel front is observed by ESEM analyses. The interface properties are established by combining the results of numerical simulations and peeling experiments at two distinct scales: the global force-displacement curves and local rubber lift geometries. The thus quantified parameters are used to predict the delamination behaviour of zigzag and horseshoe patterned interconnect structures. The accuracy of these finite element simulations is assessed by a comparison of the calculated evolution of the shape of the interconnect structures and the fibrillation areas during stretching with experimental results obtained by detailed in-situ analyses.

PACS numbers: 6835,4655,4650

Submitted to: *Journal of Physics D: Applied Physics, special cluster issue on Adhesion and Delamination of Interfaces*

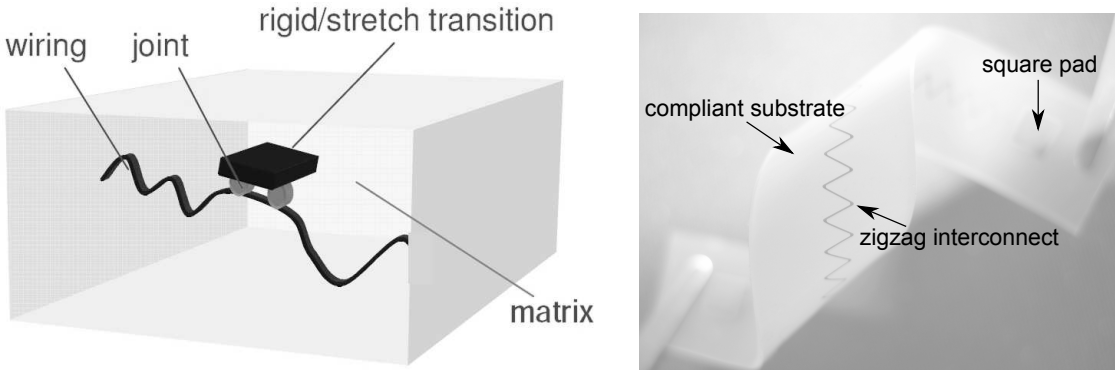

(a) (b)

Figure 1. (a) Stretchable electronics: rigid islands with brittle components in a stretchable matrix interconnected with thin metal conductor lines (from `www.stella-project.de`); (b) patterned zigzag interconnection with square pads for the electrical connection

1. Introduction

Typical examples of stretchable electronics are electronic textiles and biomedical applications, as discussed in e.g. [1, 2, 3, 4] and the recently published review paper by Rogers *et al* [5] and references therein. In order to provide conformability to the body and a high comfort during wearing, mechanical stretchability is a prerequisite for these electronics applications. In general, stretchable electronics are composed of small rigid semiconductor islands interconnected by thin metal conductor lines, see Figure 1a. The stretchability of the thin interconnects can be realized by depositing serpentine-shaped interconnects [1] on compliant flat substrates using planar patterning technologies, of which an example is shown in Figure 1b [6].

The structural reliability of the electronic circuits is one of the major concerns for stretchable electronics applications: (i) cohesive fracture of the interconnects directly leads to failure of the product due to the loss of its electrical functionality. This failure has been addressed by Li *et al* [1] and Gonzalez *et al* [4]. Here, it is conclusively shown that a serpentine shape of the metal conductor permits large deformation of the substrate while at the same time small strains are present in the metal. Hsu *et al* [7] point out that cohesive interconnect fracture is accelerated by interface failure between interconnect and substrate during stretching of fully encapsulated interconnects; (ii) adhesive fracture between the metal lines and the stretchable substrate may lead to shorts, while also the delaminated region may be a source of cohesive fracture (necking of the metal might occur, as discussed in [8, 9]) and thus electrical failure of the stretchable device.

Recently, horseshoe and zigzag interconnect patterns have been proposed as metal conductor designs [4, 6] involving in-plane patterned copper conductors onto poly(dimethylsiloxane) (PDMS) rubber flat substrates. The horseshoe shape offers high stretchability (strains up to 100% have been achieved without metal failure [7])

combined with a rather low I/O density. In contrast, the zigzag shape provides moderate stretchability (strains up to 60%) while a high I/O density can be achieved [6].

In order to understand the mechanisms leading to cohesive failure of the conducting lines, insight into the key factors that promote delamination is required [10]. For this purpose, 3D numerical models are developed to describe the delamination process during stretching. The mechanical behaviour of the PDMS rubber substrate is described by a hyperelastic model while for the copper conducting lines a nonlinear elasto-plastic model is employed. The constitutive parameters have been established by performing mechanical characterization experiments. In the finite element model, the interface behaviour is described by cohesive zone elements (see e.g. [11]). The cohesive zone properties have been characterized by means of a 90° peel test during which actual rubber fibrillation and subsequent fracture is observed. Accordingly, the cohesive zone element as formulated by Van den Bosch *et al* [12] is employed which is capable of dealing with large deformations occurring at the interface.

Although the adhesive toughness Γ_c is rather straightforward to determine from peel test experiments [13], the adhesive strength $t_{\max}$ is less obvious. In literature, the use of an extended Kalman filter [14] and variational or inverse analyses [15, 16, 17] have been proposed to extract cohesive zone parameters. In [18], the interface strength is determined by the ratio of peel force and cross-sectional area of the peel arm. Liechti and Wu [19] select the value of the maximum traction by matching experimental and numerical results of the crack-tip opening displacement fields during the initial stages of crack propagation. In this paper, a physically based approach is pursued wherein use is made of the local deformation of the compliant substrate and the copper film at the delamination front. This is achieved by combining finite element results with experimentally measured local deformations, of which first results have been reported in [20].

The thus obtained material and cohesive zone properties are then applied in the numerical models to calculate the delamination behaviour of three-dimensional horseshoe and zigzag shaped interconnects. To assess the obtained accuracy of the numerical results, the evolution of the interconnect shape during stretching is compared with in-situ SEM and optical measurements.

The paper is organized as follows: in Section 2, the mechanical properties of the metal lines and the PDMS substrate are determined from experiments. Furthermore, cohesive zone properties are established by means of 90° peel testing. In Section 3, the stretching induced delamination in the horseshoe and zigzag shape interconnect samples are predicted by means of 3D finite element simulations thereby employing the experimentally determined material and cohesive zone properties. The numerically obtained deformation behaviour of the sample designs is compared with experimental in-situ measurements. The paper ends with conclusions and recommendations in Section 4.

2. Characterization

2.1. Peel test experiments

Several testing methods are available to extract thin film interface properties and are well-documented in literature, see e.g. [13, 21, 22]. In this paper, a 90° peel test is used to establish adhesion properties. In this specific test, a thin film is peeled-off a substrate at a fixed angle of 90° from the substrate. The force is measured as a function of the clamp displacement and during peeling the force reaches a more or less constant value, called the peel force. In general, this force is dependent on film thickness, peeling angle, materials and interface properties [23]. At the steady-state delamination process, the following relation holds:

$$\Gamma_0 + \Gamma_D = \frac{P_f}{w}(1 - \cos\theta), \tag{1}$$

where Γ_0 the energy dissipation due to interface fracture (also called the intrinsic interface toughness) and Γ_D the energy dissipation due to any dissipative mechanism except interface delamination, such as plasticity [16]. Moreover, P_f is the peel force, w the width of the sample, and θ the peeling angle. When assuming that the film and substrate deform elastically, the substrate stiffness is high compared to the film stiffness, and only interface fracture contributes to dissipation, (1) reduces to

$$\Gamma_0 = \frac{P_f}{w}(1 - \cos\theta). \tag{2}$$

A more detailed treatise of film peeling can be found in [24, 13, 23].

The peel test samples studied in this paper consist of a substrate material poly(dimethylsiloxane) (PDMS) (Sylgard 186®, Dow Corning) with a copper (electrodeposited, grade TW-YE, Circuit Foil) film. The rubber is cast in a mould onto the copper film. After casting the samples are cured at room temperature. The rubber has a thickness of approximately 1.0 mm while the thickness of the copper film is 18 ± 0.5 μm, and consists of an untreated shiny side with low roughness and a treated side with high roughness values R_z ranging from 6 to 8 μm, used for improved rubber-copper adhesion; in addition an adhesion promoter is added. The samples are 84 mm in length and 18 mm in width. Prior to testing, the rubber side of the sample is glued on a metal plate that is mounted in the test set-up. For initial clamping of the sample, a part of the copper is peeled-off manually after mounting. To achieve a constant peeling angle, the device is mounted under an angle of 45° with respect to the tensile device, while the load cell is positioned perpendicular to the sample, see Figure 2a.

Even though several of the aforementioned assumptions underlying the relation between peel force and adhesion energy (2) do not hold for the studied samples, this relation is used to calculate a first estimate for the adhesion energy or work of separation Γ_c according to $\Gamma_c = P_f/w$, when assuming that the peeling angle remains approximately 90° during testing. From the resulting force-displacement curves, discussed later on in the paper and depicted in Figure 5b, the average work of separation is 1343 ± 51 $\mathrm{Jm^{-2}}$.

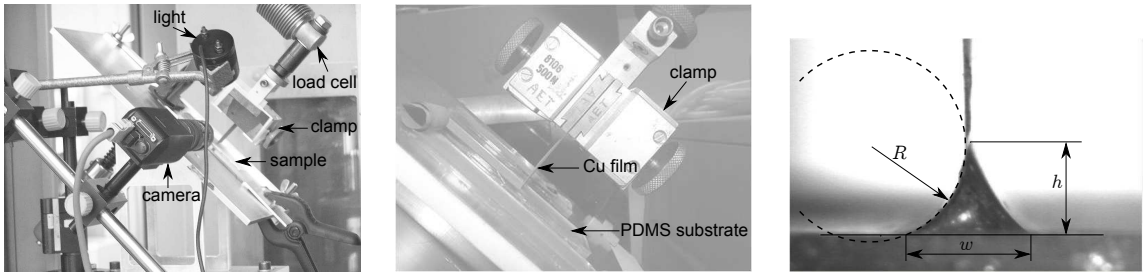

(a) (b) (c)

Figure 2. (a,b) The peel test set-up with camera to study the (c) local geometry at the delamination front with the geometry parameters

Extraction of the interface strength value from interface experiments is however not as straightforward. In literature, several approaches have been proposed to determine the interface strength value $t_{\max}$, and are mentioned in Section 1 [14, 15, 16, 17, 18, 19]. Alternatively, in this paper the local deformation of the substrate and the film is used to extract the interface strength [20]. Three local geometry parameters are defined: the width of the lifted rubber w, the height of the lifted rubber h, and the radius of the copper foil R, see Figure 2c. The width is defined as the distance between the points where the lifted rubber crosses the original rubber upper plane. The height is defined as the distance from the rubber upper plane to the top of the rubber peak. For this purpose, a camera is added to the experimental set-up, as shown in Figure 2a. The camera is fixed with respect to the metal plate on which the sample is glued, and is positioned perpendicular to the side of the sample. An example of an image recorded with the camera system of the local geometry near the delamination front during steady-state peeling is shown in Figure 2c. The averaged values over 15 measurements of different samples are: $h = 1.31 \pm 0.02$ mm, $w = 2.1 \pm 0.3$ mm, $R = 1.43 \pm 0.05$ mm. The relatively large range in the width value can be attributed to uncertainty of the position of the rubber upper plane in the images.

During peeling of the copper film from the rubber substrate, rubber fibrillation is observed at the copper-rubber interface, which is illustrated by the ESEM picture in Figure 3a. In addition, actual fracture of the rubber fibrils occurs during peel testing as evidenced by surface analysis on the copper film that reveals remaining traces of rubber after peeling, see Figure 3b. This rubber fibrillation and subsequent fracture is hypothesized to be the main explanation for the high work of separation value mentioned above. It is remarked that actual fracture toughness testing of the PDMS rubber reveals values of 16 ± 2.3 kJm^{-2}, obtained by following the test methods proposed in [25] and [26].

2.2. Determination of bulk mechanical properties

The mechanical behaviour of the silicon elastomeric rubber substrate will be described by a hyperelastic material model, commonly used to describe the nonlinear elastic

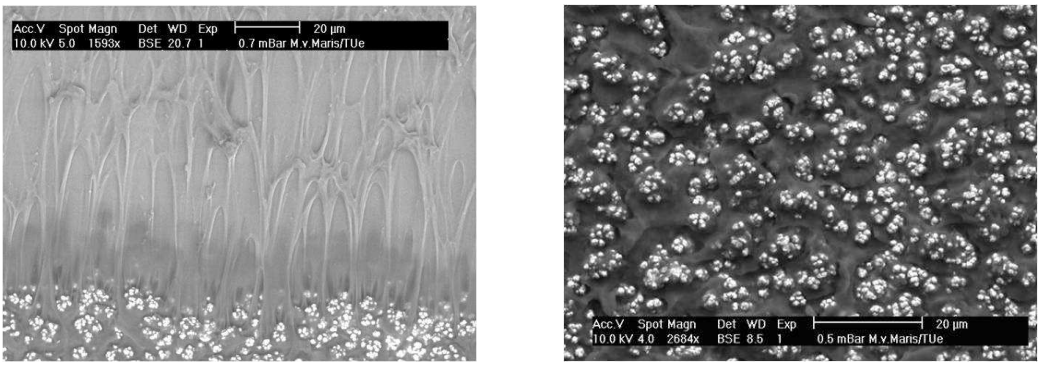

(a) (b)

Figure 3. ESEM pictures of (a) fibrillation at the copper-rubber interface during peel testing; (b) remaining PDMS (black areas) at the copper surface (light areas) after peel testing

behaviour of rubber materials at large strains. In hyperelasticity theory, the relation between the stress and strain measures is derived from the strain energy density function $W(\lambda_1, \lambda_2, \lambda_3)$ with λ_i the principal stretch ratios. It can be shown that these models exhibit real elastic behaviour meaning that no energy is dissipated. In a finite element context, no remaining stresses are present after a closed deformation path [27]. A simple neo-Hookean hyperelastic constitutive model is selected to describe the mechanical behaviour of the PDMS material as more sophisticated models did not reveal any significant improvements in their ability to match the experimental data. The strain energy equation for this model reads

$$W = C_{nH}(I_1 - 3), \tag{3}$$

in which $C_{nH} = 0.5G$ with $G = nkT$ is the rubber elastic (shear) modulus, with n the chain density, k Boltzmann's constant, T the absolute temperature, and I_1 is the first stretch invariant according to $I_1 = \lambda_1^2 + \lambda_2^2 + \lambda_3^2$. In the neo-Hookean approach, the material is assumed to be isotropic and to undergo sufficiently small deformation not to reach the finite extensibility of the rubber polymer chains. In that case, the probability distribution of chain extension is Gaussian [28]. Uniaxial tensile experiments and planar extension tests are performed under room conditions (23 ± 2°C and 50 ± 5% Relative Humidity) on a Zwick 1474 tensile testing device. To check the applicability of the neo-Hookean model, hysteresis loops are performed by loading/unloading cycles. By fitting the Neo-Hookean model on the measured uniaxial and planar extension results, a value of $C_{nH} = 0.165$ [MPa] is established, see Figure 4a. The obtained accuracy is acceptable.

The mechanical behaviour of the copper foils is described by a hypo-elasto-plastic material model including large deformations, and relies on the linear relation between the objective Jaumann rate of the Cauchy stress tensor $\overset{\circ}{\sigma}_{ij}$ and the elastic part of the

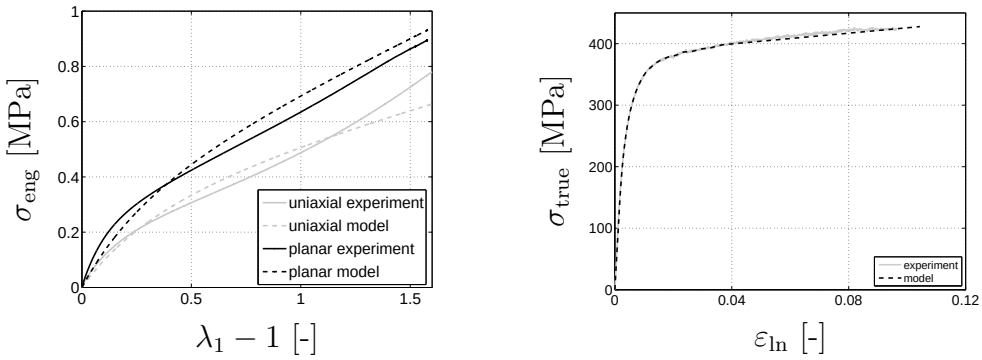

Figure 4. Measured and fitted mechanical response of (a) PDMS and (b) copper

deformation rate tensor d^e_{ij}

$$\overset{\circ}{\sigma}_{ij} = E_{ijkl}(d_{kl} - d^p_{kl}), \tag{4}$$

in which the Hookean stiffness tensor $E_{ijkl} = \mu(\delta_{ik}\delta_{jl} + \delta_{il}\delta_{jk}) + \lambda_{ijkl}$, with μ, λ Lamé's constants, and the additive decomposition of the strain rate tensor is applied, $d_{ij} = d^e_{ij} + d^p_{ij}$ [29]. The occurrence of plastic yielding depends on a yield function, denoted by $f(\sigma_{ij}, \varepsilon^p)$, where ε^p is a history parameter, in this case the total equivalent plastic strain. As is common in metal plasticity models, the deviatoric von Mises yield function is applied, expressed as

$$f = \sigma_{vm} - \varsigma(\varepsilon^p), \tag{5}$$

where $\varsigma(\varepsilon^p)$ defines the current yield stress and is determined from uniaxial tensile experiments. For more details on finite strain elasto-plasticity, the reader is referred to [30]. The experiments on the copper foils are performed under room conditions using a Kammrath & Weiss 10 kN micro-loading stage equipped with a 100 N load cell. The displacements are measured on the specimen surface by digital image correlation (DIC). Subsequently, the yield stress function $\varsigma(\varepsilon^p)$ is obtained from the measurements by converting the measured force to the Cauchy stress and the displacement to logarithmic strain values. The Cauchy stress is calculated by assuming incompressibility which is allowed due to the fact that the elastic part is very small for metals: $\sigma_{\text{true}} = (F/A_0)(L/L_0)$, with F the measured force, A_0 the initial cross section of the specimen, and L and L_0 the actual length and initial length of the specimen, respectively. The logarithmic strain is determined from $\varepsilon_{\ln} = \ln(L/L_0)$. The experimental and numerical stress-strain curves are depicted in Figure 4b. To prevent negative stiffness values during the numerical simulations, the thus determined yield curve was smoothened by removing the noise from the curve. It is remarked that a simplified isotropic model is assumed even though a columnar grain structure over the thickness of the foil was observed.

2.3. Determination of cohesive zone properties

In order to establish the cohesive zone properties Γ_c and $t_{\max}$ from the peel test, results of a finite element peel test model will be matched with experimental results. The

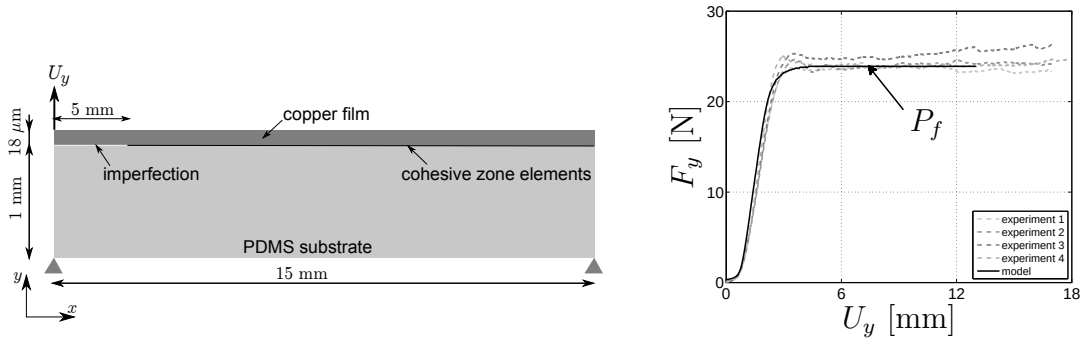

Figure 5. (a) Illustration of the peel test model (not to scale); (b) experimental and numerical force-displacement curves

geometry of the model is shown in Figure 5a. To reduce the calculation time, the length of the peel sample is taken to be 15 mm instead of the specimen length of 84 mm, which is still sufficiently large to ensure reaching the steady-state plateau value P_f. At the bottom of the substrate all degrees of freedom are suppressed, which corresponds to the experiment where the sample bottom is glued to the test setup. The peeling of the copper film is simulated by an initially delaminated region of 5 mm and prescribing a displacement in $y-$direction at the upper left corner point of the copper foil: $U_y = 13$ mm.

As already mentioned, large interface separations accompanied by fibrillation of the PDMS occur during the peel test. Therefore, the delamination process is properly captured by the large displacement cohesive zone elements as formulated by Van den Bosch *et al* [12]. In this formulation, first Piola-Kirchhoff tractions are employed. Consequently, the required cohesive zone element length corresponds to the initial element length, which can be determined unambiguously. The opening and traction vectors are no longer decomposed with respect to a local basis but resolved globally and thus, no distinction is made between normal and tangential direction. A single exponential relation between the traction t and separation δ is formulated according to

$$t = \frac{\Gamma_c}{\delta_c}\Big(\frac{\delta}{\delta_c}\Big)\exp\Big(-\frac{\delta}{\delta_c}\Big), \tag{6}$$

in which the traction vector $\vec{t} = t\vec{e}$ and the opening displacement vector $\vec{\delta} = \delta\vec{e}$, where $\vec{e}$ is the unit vector along the line between corresponding, opposite points of the interface, Γ_c the work of separation, and δ_c is the separation value at which the maximum traction $t_{\max}$ is reached, according to

$$\delta_c = \frac{\Gamma_c}{t_{\max}\exp(1)}. \tag{7}$$

Irreversibility is taken into account by assuming linear elastic unloading to the origin, i.e. elasticity-based damage. In [12], it is noted that in the case of interfacial fibrillation the presence of a traction vector parallel to the opening displacement vector and a single work-of-separation are valid assumptions, however, for other failure mechanisms this might not always be the case.

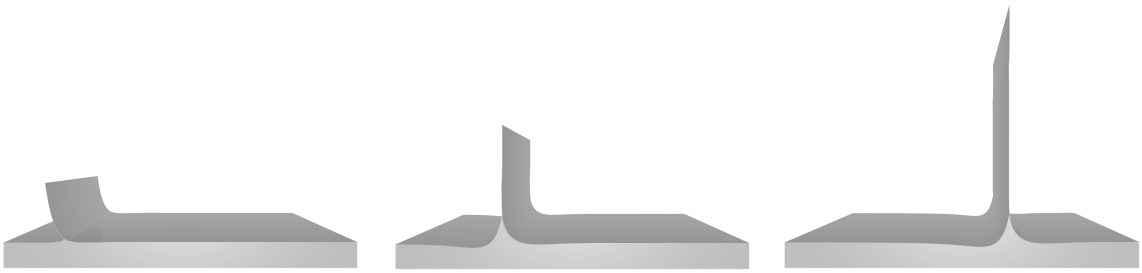

(a) (b) (c)

Figure 6. Illustration of subsequent deformation stages during peeling at a vertical displacement U_y of (a) 2.5 mm; (b) 5 mm; and (c) 10 mm for $\Gamma_c = 1330$ Jm^{-2} and $t_{\max} = 3.0$ MPa. The rubber deformation at the delamination front is apparent (for visualization purposes the cohesive zone elements and the element edges are made invisible).

In the peel test model illustrated in Figure 5a, these cohesive zone elements are located at the interface of the copper film and the rubber substrate, except at the position of the manually delaminated initial imperfection in the peel experiment. The geometry is discretized using a sufficient amount of linear quadrilateral finite elements that account for geometrical and material non-linearities, such that a unique, converged solution is obtained.

To determine the cohesive zone parameters, the work of separation Γ_c is varied between 1200 and 1400 Jm^{-2}, based on the preliminary value mentioned earlier in this section. The interface strength $t_{\max}$ is varied between 1.0 and 4.0 MPa. To illustrate the deformation behaviour of the PDMS-copper samples obtained from the numerical peel test model, Figure 6 shows typical deformation stages during loading.

Upon using Γ_c as the work of separation in the cohesive zone formulation, consequently, all dissipation processes are 'lumped' onto the cohesive zone elements except for the plastic dissipation in the copper film which is captured by the continuum plasticity model from (4) and (5), and is denoted as Γ_{CP}. Hence, this lumping approach requires the redefinition of the energy balance (1)

$$\Gamma_c = \Gamma_0 + \Gamma_D - \Gamma_{CP}. \tag{8}$$

By matching the numerical and experimental steady-state peel forces values, the critical work of separation value is obtained as $\Gamma_c = 1330$ Jm^{-2} with a resulting numerical peel force of $F_p = 24.3$ N (Figure 5b). Moreover, from the three local geometry parameters, $t_{\max}$ is obtained as $t_{\max} = 3.0$ MPa which results in $h = 1.2$ mm, $w = 1.4$ mm, and $R = 1.5$ mm. Interestingly, it is found that the effect of the value of Γ_c on the local geometry is negligible, that is, in the selected range of parameters. The dependency of the peel test results on deformation rate appears to be insignificant.

With the thus determined parameters, the critical opening can directly be obtained from (7): $\delta_c = 163$ μm. In [31], the relation between δ_c and observed fibril lengths is discussed. Although the geometry parameters are in overall agreement with the

experimental values, the following factors have a pronounced impact on these values: (i) inaccuracies in the experimental values due to the fact that a reference line for the original rubber upper plane has to be constructed to obtain the values (see Figure 2c); (ii) the neo-Hookean model does not fit the experiments exactly (see Figure 4a). In fact, it is known that the validity of the neo-Hookean model is limited to strain values up to 40%; (iii) the elasto-plastic model of the copper is isotropic while a columnar microstructure is present over the thickness of the foil; (iv) all dissipative mechanisms are lumped entirely onto the CZ elements, as formulated in (8), thereby reducing the CZ parameters to model parameters instead of intrinsic interface parameters. Although this macroscopic approach is very well suited for the analysis of the interface delamination behaviour at comparable mode angles, as can be observed from the results presented in the next section, detailed micro-mechanical analyses combined with extensive peel testing under different loading angles are required to be able to predict delamination for the whole range of mode angles.

3. Application to two characteristic three-dimensional structures

In this section, the deformation behaviour of two typical interconnect structures will be evaluated: the zigzag structure, as proposed in [6], and the horseshoe shape [4, 7]. As argued previously, the horseshoe shape offers high stretchabilities (strains up to 100% have been achieved without metal failure) combined with a rather low I/O density. In contrast, the zigzag shape provides moderate stretchability (strains up to 60%) while a high I/O density can be achieved [6].

3.1. The zigzag patterned interconnect

To predict the stretching induced delamination behaviour of the zigzag interconnect structure depicted in Figure 7a, numerical simulations are performed using the obtained material and cohesive zone properties from the preceding section. As boundary conditions, in accordance with the experiments reported in [6], a uniaxial strain of 60% is prescribed along the x-axis. The geometry of the sample is defined by the following values: $\vartheta_0 = 60°$, $\mathrm{l_{Cu}} = 2$ mm, $\mathrm{w_{Cu}} = 0.1$ mm, $\mathrm{W_S} = 10$ mm, and $\mathrm{L_S} = 8$ mm. Furthermore, the thickness of the interconnect is 18 μm, the thickness of the PDMS is 0.5 mm, while its inner and outer radii are 0.1 mm. As can be seen in the picture, the zigzag sample contains 4 zigzag interconnects. Of course, the geometry is discretized using a sufficient amount of elements such that mesh convergence is ensured: the model contains 75200 elements of which a detail is given in Figure 7b.

In order to assess the results of the numerical model, implicitly determined by the accuracy of the obtained model parameters, the evolving geometry of the interconnects during sample loading is used. In Figure 8, the simulated deformation and the corresponding in-situ optical microscope images are depicted at different deformation stages. Three geometry parameters have been defined according to Figure 8a: ϑ is the

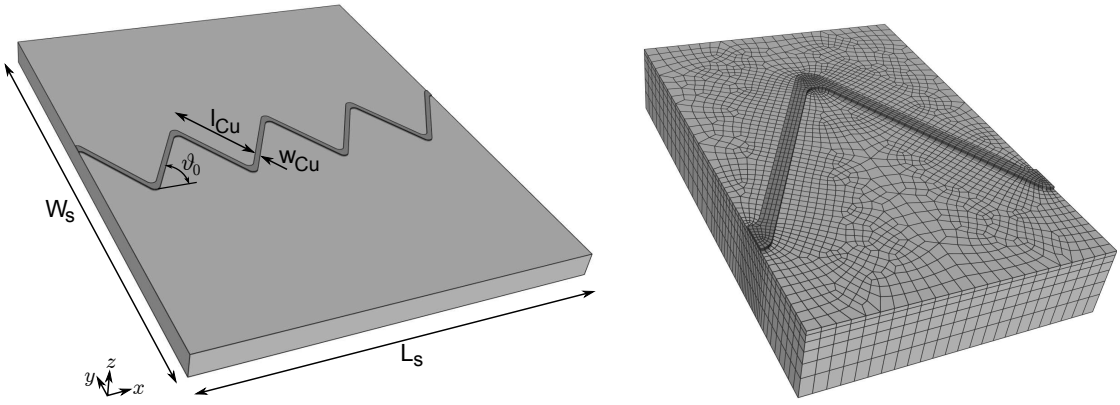

(a) (b)

Figure 7. Illustration of the patterned zigzag interconnect structure on top of the PDMS substrate: (a) entire sample; (b) mesh details of a part of the numerical model

angle of the zigzags with respect to the x-axis, b the length and w the height of the zigzag structure. However, optical inaccuracies prevent absolute comparison of these values: indeed, the measured initial value of b is 1.91 mm from the optical images while according to the specifications, this value is 2.00 mm (which is the actual value in the numerical model). Alternatively, the relative change of the geometry parameters between subsequent deformation stages is used at 25%, 50% and 60% strain, hereby implicitly assuming that the mentioned optical inaccuracies remain equal during the experiment. In Table 1, the results are given. From these results, it is found that the numerical delamination accurately captures the deformation of the interconnects during stretching as a maximum deviation of 6% is obtained.

Remarkably, the numerically predicted values are larger than the experimental values, except during the strain change from 50% to 60%. Here, the numerical values are smaller than the experimental values. During the elongation from 0 to 50%, the interconnects are deforming mainly in opening mode. During this stage, the zigzags are deforming in a more or less uniform way. It is observed that at around 60% deformation, the interconnect starts to twist in order to accommodate for the increasing deformation. This can be seen in Figure 9a: here, the local deformation and rotation below the crest is clearly visible. This increased deformation explains the higher values of the geometry parameters compared to the numerical results, in which this localized deformation appears not to be present. This can be attributed to the assumptions of the applied elasto-plastic model for the copper, as mentioned earlier.

Fibrillation of the PDMS can be observed in Figure 9a. In the numerical model this process is described by the cohesive zone elements in an averaged sense. To illustrate this, the calculated region of the deforming cohesive zone elements is identified in black in Figure 9b. It appears that the damaged or fibrillation regions are in good agreement from which it can be concluded that the lumping approach results in a meaningful, albeit averaged, description of the fibrillation process.

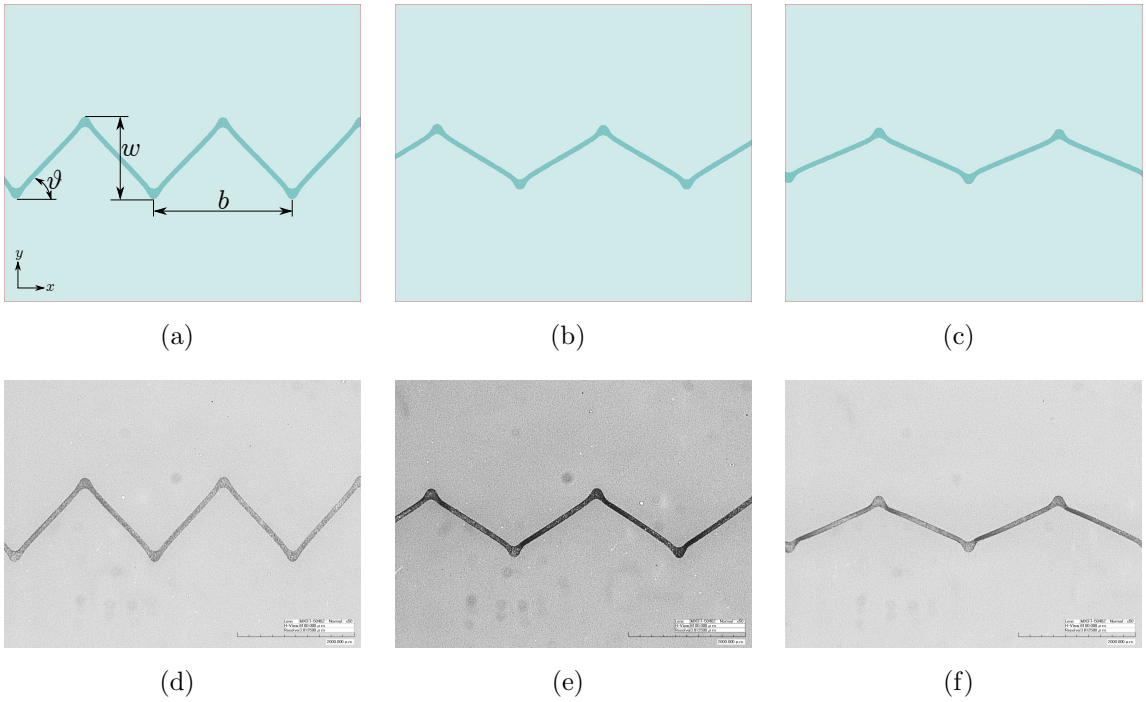

Figure 8. Deformation of the zigzag structure at a loading of 25%, 50% and 60%: (a,b,c): numerical results in which the mesh is removed for visualisation purposes; (d,e,f): micrographs from experiments. The loading is in horizontal direction.

Table 1. The relative changes of the geometrical parameters, defined in Figure 8a, between different loading stages from experimental measurements ('exp') and numerical simulations ('num')

	0 → 25% strain		25 → 50% strain		50 → 60% strain	
	exp	num	exp	num	exp	num
ϑ	20%	23%	30%	33%	31%	25%
b	25%	28%	18%	20%	8 %	6 %
w	10%	12%	19%	21%	18%	15%

3.2. The horseshoe patterned interconnect

Next, the stretching induced delamination behaviour of the horseshoe interconnect structure depicted in Figure 10a is considered. The material and interface properties and boundary conditions are similar to the zigzag structure, except that in this case, the value of the prescribed uniaxial strain is 100% along the x-axis. This is due to the fact that this structure is able to withstand larger strains before final failure occurs. The geometry of the sample is as follows: R_{Cu} = 0.75 mm, $\vartheta_0 = 120°$, w_{Cu} = 0.1 mm, W_S = 10 mm, and L_S = 10.4 mm. The thickness of the copper is 18 μm while the thickness of the PDMS is 0.5 mm. As can be seen in Figure 10a, the horseshoe sample contains 4 entire horseshoe interconnects, while mesh convergence is achieved with 82000 elements of which a detail is depicted in Figure 10b.

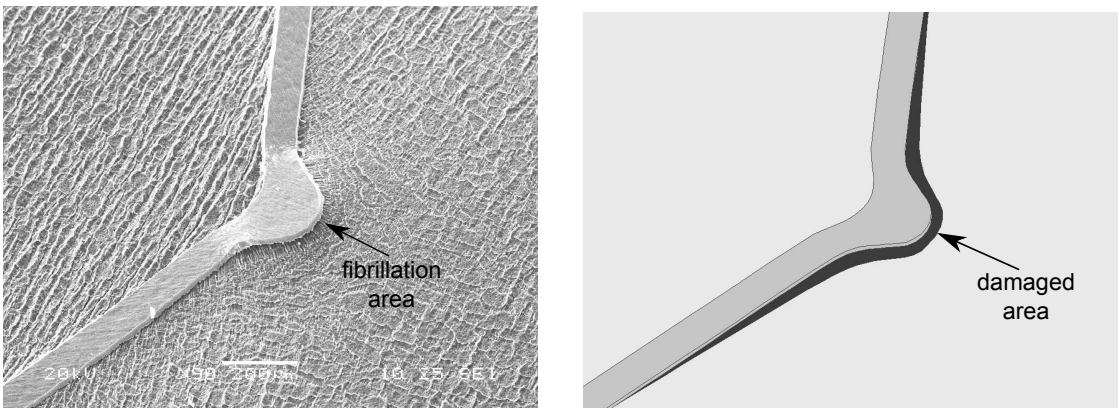

(a) (b)

Figure 9. (a) SEM micrograph after rotating and tilting the sample at 60% stretching in which the fibrillation is clearly visible; (b) the simulated result in which the black area depicts the damaged region as determined by the cohesive zone elements (the mesh is removed from the picture).

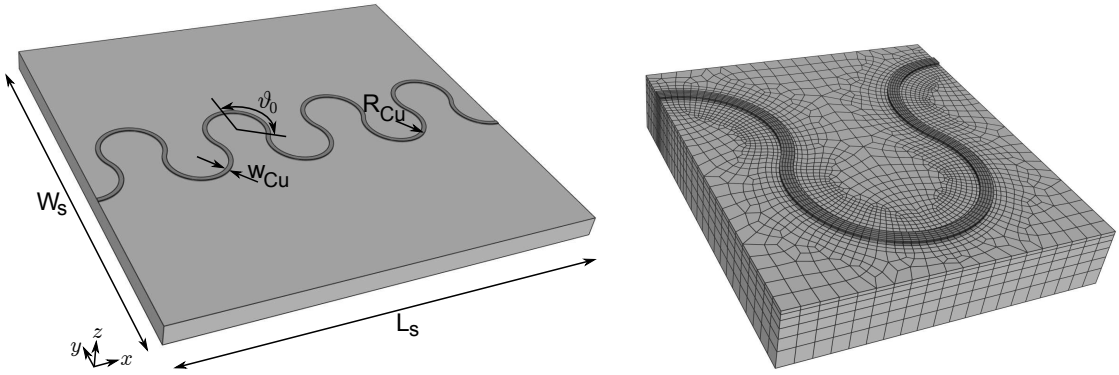

(a) (b)

Figure 10. Illustration of the patterned horseshoe interconnect structure on top of the PDMS substrate: (a) entire sample; (b) mesh details of a part of the numerical model

In Figure 11, several in-situ deformation stages obtained in the SEM are depicted. At 30% strain, only local PDMS deformation occurs around the copper layer, indicated by the arrow. Continuing to 50% strain, the PDMS stretches globally which can be concluded from the change in the surface texture of the sputtered carbon layer of a few nanometers thick. In addition, local fibrillation occurs which is however hardly visible in the picture. At 100% stretch, large-scale fibrillation takes place around the copper lines. Notice the apparent S-shaped delamination regions around the interconnects. Application of different strain rates, ranging from 0.1%sec^{-1} to 10.0%sec^{-1}, did not result in any noticeable difference in deformation of the horseshoe structures.

In order to validate the numerical model, the evolving geometry of the interconnects during sample loading is used in this case as well. However, for this geometry, it's not straightforward to define parameters that describe the interconnect geometry in a unique

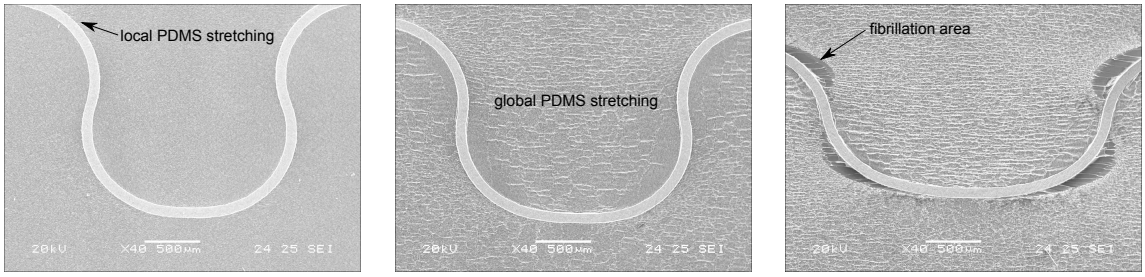

(a) (b) (c)

Figure 11. In-situ SEM images of horseshoe interconnects while stretching to (a) 30%, (b) 50%, (c) 100%

way as this shape evolves in a non-circular way. Although in [7], the horseshoe width at two different height values is considered for this purpose, in this paper a discrete geometrical description is generated from the SEM pictures by digital image processing and used instead. Consequently, coordinates of points located on the outer and inner boundaries of the horseshoes are extracted from the pictures given in Figure 11. Of course, the coordinates of these corresponding points from the numerical analyses are readily available from the simulation results. The thus extracted interconnect shapes are depicted in Figure 12. From the fact that the initial experimental and numerical shapes are almost identical (but not shown in the picture), it is concluded that this method is indeed sufficiently accurate even though extraction of the relevant coordinates from the SEM images is a manual procedure which inherently introduces a certain degree of inaccuracy. From the pictures, the stretching in horizontal direction and lateral contraction in vertical direction can be recognized. It can be concluded that a good agreement is obtained between the numerically calculated and experimentally obtained horseshoe shapes, as function of increasing stretch ratio. Noticeably, the shapes start to deviate from 80% straining. After careful inspection of the test setup, it appears that slippage at the clamps occurs which clearly explains the observed 'delay' in deformation of the horseshoes. There are several other reasons that introduce inaccuracies, which are in fact mentioned in Section 2.3, but it is believed that the occurring slippage is indeed the main reason for the observed deviation.

From Figure 11c, PDMS fibrillation is apparent. It is interesting to verify this observed fibrillation area with the numerically determined damaged zone, similar to the zigzag structure in Figure 9. In Figure 13a, the calculated damaged area is illustrated in black. From Figure 11c, it can be concluded that the damage location and shape resemble in a qualitative way. On the other hand, the experimental damage zone appears more pronounced at the sides and not present at the bottom, which is different from the numerical simulations. This can again be explained by the followed lumping approach. Another explanation is perhaps the difference in mode angles between the peel test and the actual application. The dependence of interface properties on mode angle is not considered in the current approach.

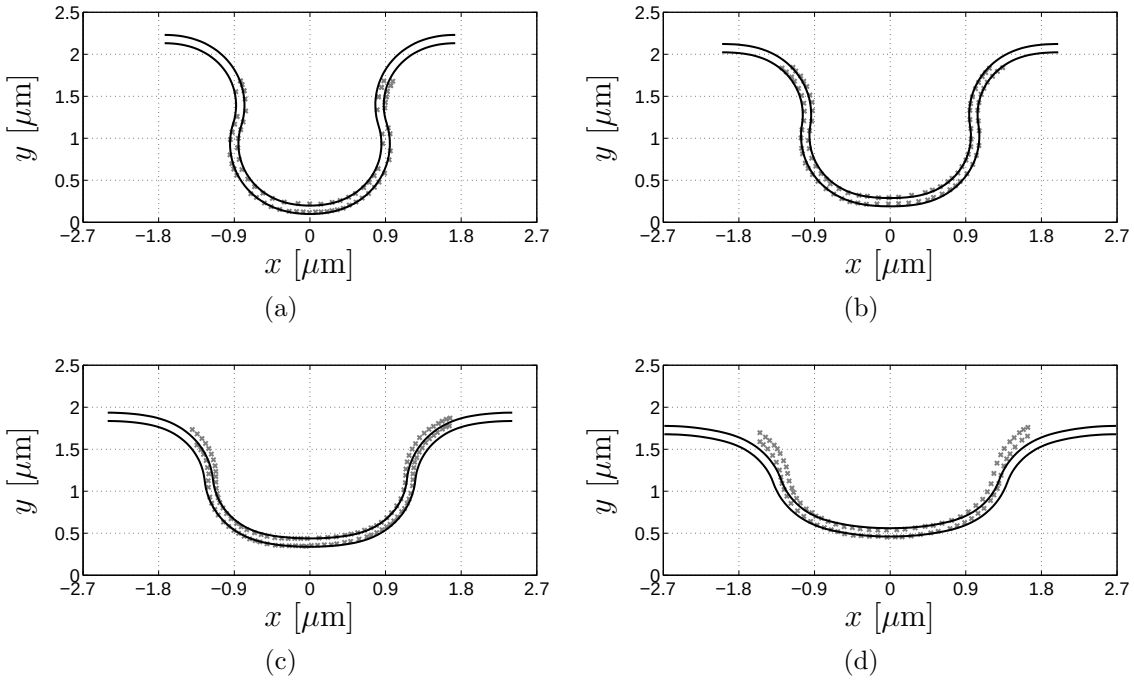

Figure 12. Deformation of the horseshoe structure at a loading of (a) 30%, (b) 50%, (c) 80%, and (d) 100%. The × symbols correspond to the interconnect outline from the SEM results while the continuous lines are results from the numerical simulations. The loading is in horizontal direction.

Figure 13. Calculated damaged area, shown in black, at 100% strain for (a) $t_{\max} = 3.0$ MPa, (b) $t_{\max} = 1.0$ MPa, (c) $t_{\max} = 4.0$ MPa

Finally, to illustrate the dependency of the damaged zone on $t_{\max}$, Figure 13b,c show the shape of the damaged zone for values of 1 MPa and 4 MPa. The lowest value results in the largest damage area while the highest strength value severely limits the damage zone in the PDMS. This confirms that the fitted value of 3 MPa yields the most realistic description of the fibrillation zone in an averaged sense.

4. Discussion

In order to predict the stretching induced interconnect delamination that might occur in stretchable electronic circuits, three-dimensional finite element models were developed.

Mechanical properties of the PDMS substrate and Cu film were determined from tensile testing from which hyperelastic and hypo-elasto-plastic material models were established, respectively. The cohesive zone parameters, used to model the transient interface delamination, were characterized by analyzing results of the 90° peel test at two distinct scales: the global force-displacement curve was used to identify the work of separation Γ_c, while local deformation measures at the delamination front were used to extract the strength value $t_{\max}$. Consequently, all dissipation mechanisms occurring during peeling of the copper are lumped onto the cohesive zone elements, including experimentally observed rubber fibrillation and subsequent fracture, but excluding the continuum plasticity, as formulated in the expression for the energy balance (8).

The thus obtained mechanical and cohesive zone properties were used to predict the stretching induced delamination of two characteristic interconnect structures: the zigzag and horseshoe designs. To validate the obtained results from the delamination models, the evolving interconnect shapes during stretching were used. For both designs, a good agreement was obtained between the experimentally measured and the numerically obtained shapes. Furthermore, the experimentally observed region in which fibrillation occurred during loading of the structure agreed well with the numerically calculated process or damaged zone in an averaged sense due to the lumping approach. The dependency of this region with respect to the value of the interface strength was illustrated.

In [31] a significant mismatch is reported between the lumped critical separation value, δ_c, and actually measured fibril lengths through in-situ microscopic measurements which is attributed to the lumping approach. Naturally, the current approach is not a-priori suited for other loading and testing conditions due to the implicit phenomenological nature. In order to identify the parameters leading to rubber fibrillation, detailed multi-scale analyses are required. Only in this case, the cohesive zone parameters correspond to the intrinsic interface properties. For instance, Lin *et al* [32] study the failure behaviour of an adhesive layer from which it is suggested that cavitation is a prerequisite to the fibrillation process. It appears that cavitation is governed by surface roughness of the opposite material (in our case, the copper film) and large hydrostatic tension in the highly constrained adhesive layer. A possible approach to consider the effect of surface roughness on adhesion properties is given in the works of Yao and Qu [33] and Noijen *et al* [34]. Supplementary to these deterministic approaches, the stochastic nature of the geometry of the roughness profiles, being of major importance on the occurring interface phenomena, could be taken into account by adopting a perturbation method within a stochastic finite element framework, as formulated in [35].

Finally, the local rubber geometry at the delamination front shown in Figure 2b suggests that delamination does not occur purely at mode 1 (i.e. opening mode). In fact, a relatively large mode 2 contribution (i.e. shear mode) is present which indicates that the interface is loaded in mixed mode. To account for this, a mode angle dependent work of separation $\Gamma_c(\psi)$, with ψ the mode angle, may have to be taken into account

for more accurate prediction of delamination phenomena in arbitrary 3D stretchable electronics designs, which can be characterized by either varying the peel angle in the current peel test or by using a dedicated mixed-mode setup, as for instance proposed in [22] and selected references therein.

Acknowledgments

The authors would like to thank Edwin van der Zanden and Marc van Maris (Eindhoven University of Technology), Sergei Shulepov and Ruud van Mullekom (Philips Applied Technologies) and Fabrice Axisa and Jan Vanfleteren (IMEC). We thank the European Commission for partial funding of this work under project Stella (IST-028026).

References

[1] T. Li, Z. Suo, S.P. Lacour, and S. Wagner. Compliant thin film patterns of stiff materials as platforms for stretchable electronics. *Journal of Materials Research*, 20:3274–3277, 2005.

[2] D.Y. Khang, H.Q. Jiang, Y. Huang, and J.A. Rogers. A stretchable form of single-crystal silicon for high-performance electronics on rubber substrates. *Science*, 311:208–212, 2006.

[3] J. Song, H. Jiang, Z.J. Liu, D.Y. Khang, Y. Huang, J.A. Rogers, C. Lu, and C.G. Koh. Buckling of a stiff thin film on a compliant substrate in large deformation. *International Journal of Solids and Structures*, 45:3107–3121, 2008.

[4] M. Gonzalez, F. Axisa, M. Vanden Bulcke, D. Brosteaux, B. Vandevelde, and J. Vanfleteren. Design of metal interconnects for stretchable electronic circuits. *Microelectronics Reliability*, 48:825–832, 2008.

[5] J.A. Rogers, T. Someya, and Y. Huang. Materials and mechanics for stretchable electronics. *Science*, 327:1603–1607, 2010.

[6] Y.Y. Hsu, M. Gonzalez, F. Bossuyt, F. Axisa, J. Vanfleteren, and I. de Wolf. In situ observations on deformation behavior and stretching-induced failure of fine pitch stretchable interconnect. *Journal of Materials Research*, 24:3573–3582, 2009.

[7] Y.Y. Hsu, M. Gonzalez, F. Bossuyt, F. Axisa, J. Vanfleteren, and I. De Wolf. The effect of pitch on deformation behavior and the stretching-induced failure of a polymer-encapsulated stretchable circuit. *Journal of Micromechanics and Microengineering*, 20:075036, 2010.

[8] T. Li and Z. Suo. Ductility of thin metal films on polymer substrates modulated by interfacial adhesion. *International Journal of Solids and Structures*, 44:1696–1705, 2007.

[9] N. Lu, X. Wang, Z. Suo, and J. Vlassak. Metal films on polymer substrates stretched beyond 50%. *Applied Physics Letters*, 91:221909, 2007.

[10] N. Lu, J. Yoon, and Z. Suo. Delamination of stiff islands patterned on stretchable substrates. *International Journal of Materials Research*, 98:717–721, 2007.

[11] M. Ortiz and A. Pandolfi. Finite-deformation irreversible cohesive elements for three-dimensional crack-propagation analysis. *International Journal for Numerical Methods in Engineering*, 44:1267–1282, 1999.

[12] M.J. van den Bosch, P.J.G. Schreurs, and M.G.D. Geers. A cohesive zone model with a large displacement formulation accounting for interfacial fibrilation. *European Journal of Mechanics A/Solids*, 26:1–19, 2007.

[13] L.B. Freund and S. Suresh. *Thin film materials; Stress, defect formation and surface evolution.* Cambridge University Press, 2006.

[14] A. Corigliano and S. Mariani. Parameter identification of a time-dependent elastic-damage interface model for the simulation of debonding in composites. *Composites Science and Technology*, 61:191–203, 2001.

[15] T. Ferracin, C.M. Landis, F. Delannay, and T. Pardoen. On the determination of the cohesive zone properties of an adhesive layer from the analysis of the wedge-peel test. *International Journal of Solids and Structures*, 40:2889–2904, 2003.

[16] H. Zhao and Y. Wei. Determination of interface properties between micron-thick metal film and ceramic substrate using peel test. *International Journal of Fracture*, 144:103–112, 2007.

[17] P.A. Gustafson and A.M. Waas. The influence of adhesive constitutive parameters in cohesive zone finite element models of adhesively bonded joints. *International Journal of Solids and Structures*, 46:2201–2215, 2009.

[18] G. Geißler and M. Kaliske. Peel process simulation of sealed polymeric film computational modelling of experimental results. *Engineering Computations: International Journal for Computer-Aided Engineering and Software*, 24:586–607, 2007.

[19] K.M. Liechti and J-D. Wu. Mixed-mode, time-dependent rubber/metal debonding. *Journal of the Mechanics and Physics of Solids*, 49:1039–1072, 2001.

[20] O. van der Sluis, P.H.M. Timmermans, E.J.L. van der Zanden, and J.P.M. Hoefnagels. Analysis of the three-dimensional delamination behavior of stretchable electronics applications. In M.H. Aliabadi, S. Abela, S. Baragetti, M. Guagliano, and H-S. Lee, editors, *Key Engineering Materials*, volume 417–418, pages 9–12. Trans Tech Publications, 2010. Special volume: Advances in Fracture and Damage Mechanics VIII, ISSN 1013–9826.

[21] A.A. Volinksy, N.R. Moody, and W.W. Gerberich. Interfacial toughness measurements for thin films on substrates. *Acta Materialia*, 50:441–466, 2002.

[22] M. Kolluri, M.H.L. Thissen, J.P.M. Hoefnagels, J.A.W. van Dommelen, and M.G.D. Geers. In-situ characterization of interface delamination by a new miniature mixed mode bending setup. *International Journal of Fracture*, 158:183–195, 2009.

[23] M.D. Thouless and Q.D. Yang. A parametric study of the peel test. *International Journal of Adhesion and Adhesives*, 28:176–184, 2008.

[24] K-S. Kim and N. Aravas. Elastoplastic analysis of the peel test. *International Journal of Solids and Structures*, 24:417–435, 1988.

[25] R.S. Rivlin and A.G. Thomas. Rupture of rubber. I. Characteristic energy for tearing. *Journal of Polymer Science*, 10:291–318, 1953.

[26] B.H. Kim and C.R. Joe. Single specimen test method for determining fracture energy (J_c) of highly deformable materials. *Engineering Fracture Mechanics*, 32:155–161, 1989.

[27] G. Weber and L. Anand. Finite deformation constitutive equations and a time integration procedure for isotropic, hyperelastic-viscoplastic solids. *Computer Methods in Applied Mechanics and Engineering*, 79:173–202, 1990.

[28] I.M. Ward and J. Sweeney. *An Introduction to the Mechanical Properties of Solid Polymers*. John Wiley & Sons: Chichester, U.K., 2004.

[29] S. Nemat-Nasser. On finite deformation elasto-plasticity. *International Journal of Solids and Structures*, 18:857872, 1982.

[30] J.C. Simo and T.J.R. Hughes. *Computational Inelasticity*. Interdisciplinary Applied Mathematics. Springer-Verlag, New York, 1998.

[31] J.P.M. Hoefnagels, J. Neggers, P.H.M. Timmermans, O. van der Sluis, and M.G.D. Geers. Copper-rubber interface delamination in stretchable electronics. *Scripta Materialia*, 63:875–878, 2010.

[32] Y.Y. Lin, C.Y. Hui, and Y.C. Wang. Modeling the failure of an adhesive layer in a peel test. *Journal of Polymer Science: Part B: Polymer Physics*, 40:2277–2291, 2002.

[33] Q. Yao and J. Qu. Interfacial versus cohesive failure on polymer-metal interfaces in electronic packaging–effects of interface roughness. *Journal of Electronic Packaging*, 124:127–134, 2002.

[34] S.P.M. Noijen, O. van der Sluis, P.H.M. Timmermans, and G.Q. Zhang. Numerical prediction of failure paths at a roughened metal/polymer interface. *Microelectronics Reliability*, 49:1315–1318, 2009.

[35] M.A. Gutierrez and S. Krenk. Stochastic finite element methods. In E. Stein, R. de Borst, and T.J.R. Hughes, editors, *Encyclopedia Of Computational Mechanics*, volume 2, pages 657–681.

John Wiley & Sons, Ltd, Chichester, 2004.